ÉCOLE POLYTECHNIQUE FÉDÉRALE DE LAUSANNE
MATHICSE
Institute of Mathematics
School of Basic Sciences

MATHICSE Technical Report
Nr. 10.2017
May 2017


# Continuation Multi-Level Monte-Carlo method for Uncertainty Quantification in Turbulent Compressible Aerodynamics Problems modeled by RANS

Michele Pisaroni, Fabio Nobile, Penelope Leyland

http://mathicse.epfl.ch

Address: EPFL - SB – INSTITUTE OF MATHEMATICS – Mathicse
(Bâtiment MA) Station 8 - CH-1015 - Lausanne - Switzerland

# Continuation Multi-Level Monte-Carlo method for Uncertainty Quantification in Turbulent Compressible Aerodynamics Problems modeled by RANS

Michele Pisaroni[a], Fabio Nobile[a], Penelope Leyland[a]

[a] *École polytechnique fédérale de Lausanne, MATH CSQI, Station 8, 1015 Lausanne, Switzerland*

**Abstract**

In this technical report we apply the Continuation Multi Level Monte Carlo (C-MLMC) algorithm presented in [1] to efficiently propagate operating and geometric uncertainties in internal and external aerodynamic simulations modeled by RANS. In particular, we discuss the construction of suitable mesh hierarchies and test the C-MLMC algorithm on the 2D RAE-2822 transonic airfoil and the 3D NASA Rotor 37 affected by operating uncertainties.

*Keywords:* Multi Level Monte Carlo, Uncertainty Quantification, Aerodynamics, Turbulent Flows.

## 1. Introduction

Uncertainty Quantification (UQ) has become nowadays an essential ingredient in aerodynamic robust design and optimization. Despite the advances in computational fluid dynamics (CFD) and the wide availability of modern parallel computer architectures, the efficient propagation of uncertainties in model parameters (such as operating conditions and geometrical parameters) to quantities of interest (QoI) for the problem under investigation is still a significant challenge, especially when many sources of uncertainties are present and when each deterministic realization requires the solution of high-fidelity models with many degrees of freedom.

The geometrical and operational parameters that characterize aerodynamic systems in mathematical and computational models are naturally affected by aleatory uncertainties due to the intrinsic variability of manufacturing processes and the surrounding environment. These uncertainties have to be taken into account to achieve and guarantee the highest safety standards and to design aerodynamic systems whose performance are unchanged when exposed to variabilities.

In this technical report, we revisit the C-MLMC algorithm presented in [1, 2] and particularize it to the specific setting of viscous compressible aerodynamics simulations modeled by RANS affected by operational and geometrical uncertainties. We briefly recall here the C-MLMC algorithm, referring to [1] for a detailed description, and focus in this work on its application of the algorithm to specific external and internal aerodynamics benchmark test cases defined during the European Union's FP7 project UMRIDA (Uncertainty Management for Robust Industrial Design in Aeronautics (UMRIDA), namely the transonic RAE 2822 airfoil and the NASA Rotor 37. In particular, we detail how we have constructed the grid hierarchy for the two problems that provides appropriate grid convergence rates for the C-MLMC to be effective. For the RAE-2822 problem we provide also a comparison with a standard Monte Carlo method which shows a huge speedup in terms of computational complexity.

This report is organized as follows. Section 3 recalls the MLMC method for scalar and scalar fields QoI. In Section 3 we explain how to calibrate the C-MLMC to compute expectations of such QoI. Section 4 presents

*Corresponding author

*Email address:* michele.pisaroni@epfl.ch (Michele Pisaroni)

the model problems and the results of the stochastic analysis performed on the NASA Rotor-37 and the RAE-2822 airfoil.

## 2. Multi Level Monte Carlo

We consider a compressible viscous aerodynamic problem modeled by the RANS equations, where some parameters (e.g. angle of attack, Mach number, profile of an airfoil) are partially unknown and described as random variables with a given probability law. We denote by $u = u(\omega)$ its solution, where $\omega$ denotes a random elementary event. Our goal is to compute the expected value $\mathbb{E}[Q]$ of a quantity of interest (QoI) $Q = f(u)$. Examples of QoI are the lift coefficient $C_L$ of an airfoil or the isentropic efficiency of a rotor. The key idea of classical Multi Level Monte Carlo (MLMC) is to simultaneously draw MC samples on several approximations $Q_{M_l}$ of a quantity of interest (QoI) $Q$ built on a hierarchy of computational grids (with discretization parameters $M_0 < M_1 < \cdots < M_L = M$). For the sake of explanation, we recall the MLMC estimator for $\mathbb{E}[Q]$:

$$\mathtt{E}^{\mathtt{MLMC}}[Q_M] := \sum_{l=0}^{L} \frac{1}{N_l} \sum_{i=1}^{N_l} Y_l(\omega^{(i,l)}) = \sum_{l=0}^{L} \mathtt{E}^{\mathtt{MC}}[Q_{M_l} - Q_{M_{l-1}}], \tag{1}$$

The accuracy in estimating $\mathbb{E}[Q]$ by $\mathtt{E}^{\mathtt{MLMC}}[Q_M]$ can be quantified by considering the mean square error (MSE) of the estimator:

$$e(\mathtt{E}^{\mathtt{MLMC}}[Q_M])^2 := \mathbb{E}[(\mathtt{E}^{\mathtt{MLMC}}[Q_M] - \mathbb{E}[Q])^2] = \underbrace{\left(\mathbb{E}[Q_M - Q]\right)^2}_{(\text{B-}\mathtt{E}^{\mathtt{MLMC}})} + \underbrace{\sum_{l=0}^{L} \frac{\mathbb{V}\mathrm{ar}[Y_l]}{N_l}}_{(\text{SE-}\mathtt{E}^{\mathtt{MLMC}})}. \tag{2}$$

To tune the MLMC algorithm one needs to estimate how the error and cost depend on the number of degrees of freedom (DoF) $M_l$ on each level, for a given hierarchy of meshes. Namely one needs to estimate the following constants and rates $\mathcal{P} = \{c_\alpha, \alpha, c_\beta, \beta, c_\gamma, \gamma\}$ such that:

**a1.** The cost to compute one sample $Q_{M_l}$ at level $l$ is:

$$Cost(Q_{M_l}(\omega^{(i)})) \leq c_\gamma M_l^\gamma, \tag{3}$$

**a2.** $\mathbb{E}[Q_{M_l}]$ converges to $\mathbb{E}[Q]$ with rate $\alpha$ w.r.t. $M_l$, i.e.:

$$|\mathbb{E}[Q_{M_l} - Q]| \leq c_\alpha M_l^{-\alpha} \tag{4}$$

for some $c_\alpha, \alpha > 0$

**a3.** $\mathbb{V}\mathrm{ar}[Y_l]$ decays with rate $\beta$ w.r.t. $M_l$ i.e.:

$$\mathbb{V}\mathrm{ar}[Y_l] \leq c_\beta M_l^{-\beta}, \tag{5}$$

for some $c_\beta, \beta > 0$ and $\alpha \geq \min(\beta, \gamma)$.

We introduce a splitting parameter $\theta \in (0, 1)$ (usually taken as $\theta = \frac{1}{2}$) and require in our simulations that:

$$Bias: \quad \mathbf{B} := |\mathbb{E}[Q] - \mathbb{E}[Q_M]| \leq \ (1-\theta)\varepsilon, \tag{6a}$$

$$Statistical\ Error: \quad \mathbf{SE} := \mathbb{V}ar[\mathtt{E}^{\mathtt{MLMC}}[Q_M]] = \sum_{l=0}^{L} \frac{\mathbb{V}ar[Y_l]}{N_l} \leq \theta(2-\theta)\varepsilon^2 \tag{6b}$$

so that the MSE:

$$e(\mathtt{E}^{\mathtt{MLMC}}[Q_M]) = \mathbf{B}^2 \ + \ \mathbf{SE} \leq \varepsilon^2 \tag{7}$$

From (4), the bias constraint (6a) is satisfied by choosing:

$$L = L(\varepsilon): \ M_{L(\varepsilon)} \geq \left( \frac{(1-\theta)\varepsilon}{c_\alpha} \right)^{-\frac{1}{\alpha}} \tag{8}$$

On the other hand, following the optimization argument in [3], the statistical error constraint (6b) is satisfied by choosing:

$$N_l(\varepsilon) = \left\lceil \left( \frac{1}{\theta(2-\theta)\varepsilon^2} \right) \sqrt{\frac{\mathbb{V}ar[Y_l]}{C_l}} \sum_{k=0}^{L} \sqrt{C_k \mathbb{V}ar[Y_k]} \right\rceil \tag{9}$$

In practical aerodynamic applications we are usually required to compute quantities of interest $\mathcal{Q}(x,\omega)$ that are scalar fields defined on a certain domain $D$ (e.g. pressure coefficient around an airfoil). In this case we enforce the MSE to be smaller than $\varepsilon^2$, where in the definition of the MSE, we measure for convenience the spatial error in the $L^2$ norm (mean-square sense) [4].

$$\begin{aligned} e(\mathtt{E}^{\mathtt{MLMC}}[\mathcal{Q}_M])^2 :=& \mathbb{E}[\|\mathtt{E}^{\mathtt{MLMC}}[\mathcal{Q}_M] - \mathbb{E}[\mathcal{Q}]\|^2_{L^2(D)}] \\ =& \underbrace{\|\mathbb{E}[\mathcal{Q}_M - \mathcal{Q}]\|^2_{L^2(D)}}_{(\text{B-}\mathtt{E}^{\mathtt{MLMC}})} + \underbrace{\sum_{l=0}^{L} \frac{1}{N_l} \|\mathbb{V}\text{ar}[\mathcal{Y}_l]\|_{L^1(D)}}_{(\text{SE-}\mathtt{E}^{\mathtt{MLMC}})}. \end{aligned} \tag{10}$$

where $\mathcal{Y}_l = \mathcal{Q}_{M_l} - \mathcal{Q}_{M_{l-1}}$.

Following the same arguments presented above we enforce:

$$Bias: \quad \mathbf{B} := \|\mathbb{E}[\mathcal{Q}_M - \mathcal{Q}]\|_{L^2(D)} \leq \ (1-\theta)\varepsilon, \tag{11a}$$

$$Statistical\ Error: \quad \mathbf{SE} := \mathbb{V}ar[\mathtt{E}^{\mathtt{MLMC}}[\mathcal{Q}_M]] = \sum_{l=0}^{L} \frac{\|\mathbb{V}\text{ar}[\mathcal{Y}_l]\|_{L^1(D)}}{N_l} \leq \theta(2-\theta)\varepsilon^2 \tag{11b}$$

From (4), the bias constraint (11a) is satisfied by choosing $L$ as in (8) and the statistical error constraint (11b) is satisfied by choosing:

$$N_l = \left\lceil \left( \frac{1}{\theta(2-\theta)\varepsilon^2} \right) \sqrt{\frac{\|\mathbb{V}\text{ar}[\mathcal{Y}_l]\|_{L^1(D)}}{C_l}} \sum_{k=0}^{L} \sqrt{C_k \|\mathbb{V}\text{ar}[\mathcal{Y}_l]\|_{L^1(D)}} \right\rceil \tag{12}$$

Given a hierarchy of discretizations with $M_0 < M_1 < \ldots$, from the practical point of view the standard MLMC algorithm is generally composed of four steps:

1. Theoretical or computational estimation of the problem dependent rates and constants ($\mathcal{P} = \{c_\alpha, \alpha, c_\beta, \beta, c_\gamma, \gamma\}$)
2. Estimation of $\mathbb{V}ar[Y_l]$ (or $\|\mathbb{V}\text{ar}[\mathcal{Y}_l]\|_{L^1(D)}$ in case of scalar field) .
3. Estimation of the optimal number of levels $L$ from (8) and sample sizes $N_l$ from (9) (or (12) in case of scalar field).
4. Run the hierarchy $\{0, \ldots, L\}$ with an optimal $\{N_l\}_{l=0}^{L}$

Theoretical estimates for the rates $\alpha$ and $\beta$ exist for certain classes of PDEs with random parameters [5, 6, 7, 8] and depend on the smoothness of the data of the problem as well as the smoothing proprieties of the differential operator. On the other hand the parameter $\gamma$ depends on the number of spatial dimensions of the deterministic problem and the efficiency of the deterministic solver.

The total cost of MLMC strongly depends also on the problem dependent constants $c_\alpha, c_\beta, c_\gamma$ as they enter in the choice of the optimal parameters $L$, $\{N_l\}_{l=0}^L$, and these have to be estimated numerically as accurately as possible. The common practice is to compute the rates and the constants by performing an initial *screening* over the first few levels $\{0, \dots, \overline{L}\}$ with a predefined sample size $\overline{N}$ and fit the rates and constants via a least squares procedure.

The main drawback of this procedure is that for computationally expensive problems, this screening phase, whose cost is usually not accounted for in the literature, can be quite time consuming. In particular, if $\overline{L}$ and $\overline{N}$ are chosen too large the screening phase might turn out to be more expensive than the overall MLMC simulation on the optimal hierarchy $\{0, \dots, L\}$. On the other hand, if $\overline{L}$ and $\overline{N}$ are chosen too small, the extrapolation of the convergence rates $\alpha$ and $\beta$ on finer levels might be quite unreliable.

## 3. Continuation Multi Level Monte Carlo

To overcome the above mentioned limitations of the standard MLMC algorithm concerning the screening phase we consider here the Continuation Multi Level Monte Carlo (CMLMC) algorithm presented in [1] for compressible inviscid aerodynamics problems inspired from [2]. The key idea of CMLMC is to solve for the QoI with a sequence of decreasing tolerances and progressively improve the estimation of the problem dependent parameters $\mathcal{P}$ that, as presented before, directly control the number of levels and sample sizes. To achieve a certain RMSE of $\varepsilon$, we set a slightly smaller tolerance $\frac{\varepsilon}{r_2}$ with $r_2 > 1$ and define a sequence of decreasing tolerances $\varepsilon_0 > \varepsilon_1 > \cdots > \varepsilon_i > \cdots > \varepsilon_k = \frac{\varepsilon}{r_2}$ with $\varepsilon_i = r_1 \varepsilon_{i+1}$ where, for a given $\varepsilon_0 > \varepsilon$, the number $k$ of iterations is given by:

$$k = \left\lfloor \frac{-log(\frac{\varepsilon}{r_2}) + log(\varepsilon_0)}{log(r_1)} \right\rfloor. \tag{13}$$

Eventually, we might still run the algorithm for few more iterations with tolerances $\varepsilon_{k+j} = \frac{\varepsilon_k}{r_2 j}$ until the actual estimated RMSE is below $\varepsilon$.

The essential feature of the CMLMC with respect to standard MLMC algorithm is that the parameter set $\mathcal{P}$ is computed on-the-fly and updated at each iteration of the algorithm. The estimation of the parameters that describe the cost $(c_\gamma, \gamma)$ and the bias $(c_\alpha, \alpha)$ is relatively straightforward since these quantities can be estimated also with just few realizations per level. The estimation of the variances $\mathbb{V}ar[Y_l]$, on the other hand, can be quite inaccurate with a small sample size. In a standard MLMC such variances are usually computed using a sample variance estimator:

$$\mathbb{V}ar[Y_l] \approx \mathtt{V}^{\mathtt{MC}}[Y_l] = \frac{1}{N_l - 1} \sum_{n=1}^{N_l} \left( Y_l(\omega^{(n,l)}) - \mathtt{E}^{\mathtt{MC}}[Y_l] \right)^2 \tag{14}$$

At the deepest levels usually we do not have enough realizations to accurately compute $\mathtt{V}^{\mathtt{MC}}[Y_l]$ (asymptotically accurate only as $N_l \to \infty$ ) and estimate the sample sizes $N_l$ for the next iteration, as well as the parameters $(c_\beta, \beta)$ needed to extrapolate $\mathbb{V}ar[Y_l]$ hence $N_l$ on new levels that are added at the next iteration. Using the bias model $\mathbb{E}[Y_l] \approx \widehat{\mu}_l := c_\alpha M_l^{-\alpha}$ and variance model $\mathbb{V}ar[Y_l] \approx \widehat{\lambda}_l^{-1} := c_\beta M_l^{-\beta}$ with $c_\alpha, \alpha, c_\beta, \beta$ estimated from the previous iteration of the CMLMC algorithm. The idea is to describe $Y_l$ as a Gaussian random variable $\mathcal{N}(\mu_l, \lambda_l^{-1})$ and perform a Bayesian update of $\mu_l$ and $\lambda_l^{-1}$ based on the collected values $Y_l(\omega^{(n,l)})$ and a Normal-Gamma prior distribution with maximum at $\widehat{\mu}_l$ and $\widehat{\lambda}_l$. The posterior is also a Normal-Gamma, with maximum at

$$\mu_l^{MAP} = \frac{N_l \mathtt{E}^{\mathtt{MC}}[Y_l] + k_0 \widehat{\mu}_l}{k_0 + N_l} \qquad \text{and} \qquad \lambda_l^{MAP} = \frac{\Xi_{1,l} - \frac{1}{2}}{\Xi_{2,l}} \tag{15}$$

with:

$$\Xi_{1,l} = \frac{1}{2} + k_1\widehat{\lambda}_l + \frac{N_l}{2}, \tag{16a}$$

$$\Xi_{2,l} = k_1 + \frac{N_l - 1}{2}\mathtt{V}^{\mathtt{MC}}[Y_l] + \frac{k_0 N_l(\mathtt{E}^{\mathtt{MC}}[Y_l] - \widehat{\mu}_l)^2}{2(k_0 + N_l)}. \tag{16b}$$

The parameters $k_0$ and $k_1$ represent our 'certainty' on $\widehat{\mu}_l$ and $\widehat{\lambda}_l^{-1}$. The resulting update formula for $\mathbb{V}ar[Y_l] \approx \lambda_l^{-1}$ is then:

$$\mathtt{V}^{\mathtt{C}}[Y_l] := \frac{\Xi_{2,l}}{\Xi_{1,l} - \frac{1}{2}} \qquad l > 0 \tag{17}$$

Finally, following the above arguments, we approximate the variance of the MLMC estimator as:

$$\mathbb{V}ar[\mathtt{E}^{\mathtt{MLMC}}[Q_M]] = \sum_{l=0}^{L} \frac{\mathbb{V}ar[Y_l]}{N_l} \approx \sum_{l=0}^{L} \frac{\mathtt{V}^{\mathtt{C}}[Y_l]}{N_l} \tag{18}$$

## 4. Model Problems

We consider turbulent compressible flows modeled by the Favre-averaged (density-weighted average $\tilde{f} = \overline{\rho f}/\overline{\rho}$) Navier-Stokes equations [9, 10]:

$$\frac{\partial \overline{\rho}}{\partial t} + \frac{\partial}{\partial x_i}\left(\overline{\rho}\tilde{u}_i\right) = 0, \tag{19a}$$

$$\frac{\partial}{\partial t}\left(\overline{\rho}\tilde{u}_i\right) + \frac{\partial}{\partial x_j}\left(\overline{\rho}\tilde{u}_i\tilde{u}_j\right) = -\frac{\partial p}{\partial x_i} + \frac{\partial \overline{\sigma}_{ij}}{\partial x_j} + \frac{\partial \tau_{ij}}{\partial x_j} \tag{19b}$$

$$\frac{\partial}{\partial t}\left(\overline{\rho}\tilde{E}\right) + \frac{\partial}{\partial x_j}\left(\overline{\rho}\tilde{u}_j\tilde{H}\right) = \frac{\partial}{\partial x_j}\left[\tilde{u}_i\overline{\sigma}_{ij} + \overline{\sigma_{ij}u_i''}\right] \tag{19c}$$

$$+ - \frac{\partial}{\partial x_j}\left[-q_j + c_p\overline{\rho u_j'' T''} - \tilde{u}_i\tau_{ij} + \frac{1}{2}\overline{\rho u_i'' u_i'' u_j''}\right] \tag{19d}$$

where we denote with $\tau_{ij} = -\overline{\rho u_i'' u_j''}$ the Reynolds stress term and $\overline{\sigma}_{ij}$ the viscous stress tensor. The former is approximated by solving the Spalart-Allmaras turbulence model with quadratic constitutive relation [11]. We approximate the turbulent heat flux $c_p\overline{\rho u_j'' T''} \approx -\frac{c_p\tilde{\mu}_t}{Pr_t}\frac{\partial \tilde{T}}{\partial x_j}$ following a Reynolds analogy and we use a constant turbulent Prandtl number $Pr_t = 0.9$. The Sutherland's Law is employed to compute the dynamic viscosity from the temperature of the ideal gas ($Pr = 0.72$).

The above mentioned equations are discretized on structured grids (finite volume method) and advanced in time using a fully implicit time stepping scheme. Local time-stepping and algebraic multigrid (AMG) are used for convergence acceleration to the steady-state solution.

### *4.1. Model Problems: NASA ROTOR-37*

The first problem we consider is the well established turbomachinery test case NASA ROTOR-37 (UMRIDA BC-01), a transonic axial flow compressor. The rotor has 36 blades and an aspect ratio of 1.19, rotates at 17188.7 $[rpm]$ (1800 $[rad/s]$), leading to a tip-speed of 454 $[m/s]$. A detailed description of the geometry, the original experimental set-up and a series of simulations can be found in [12, 13].

The design parameters of the rotor are summarized in the following Table 1:

| Quantity | Symbol | Design Value |
|---|---|---|
| Rotor Total Pressure Ratio | $P_2/P_1$ | 2.106 |
| Rotor Total Temperature Ratio | $T_2/T_1$ | 1.270 |
| Rotor Adiabatic Efficiency | $\eta_{ad}$ | 0.877 |
| Mass Flow $[kg/s]$ | $\dot{m}$ | 20.188 |

Table 1: Design values for the NASA ROTOR-37 problem.

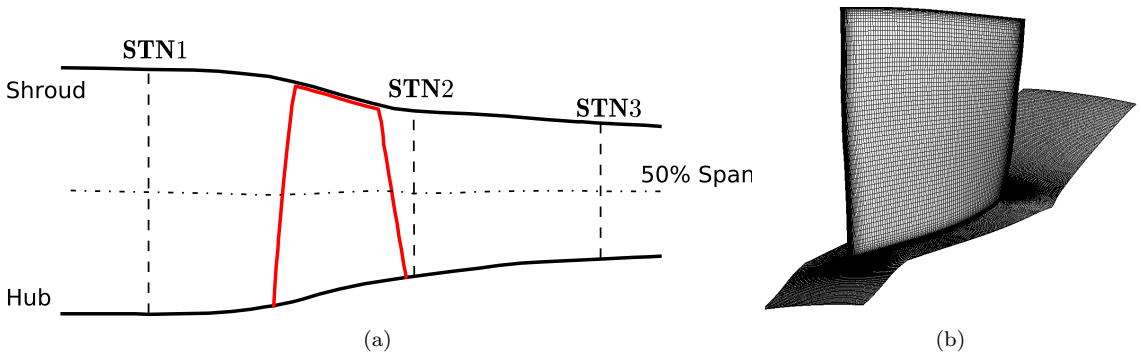


Figure 1: (a) NASA Rotor 37 and (b) computational model

*4.1.1. Determinsitic results*

The computational model (Fig.1(b)) consists of one blade with periodic boundary conditions. The rotation is imposed to the hub and the blade, while the shroud is kept fixed. Total pressure and total temperature profiles derived from experiments [12] are imposed at the inlet boundary and the static pressure is varied at the outlet to change the mass flow.

The proprieties of the multi-block structured 4-levels grid hierarchy used in the C-MLMC, generated using NUMERCA Autogrid, are presented in the following Table 2 along with the average computational time required to compute one deterministic simulation using CFD++ software environment.

| LEVEL | Blade nodes | Spanwise nodes | Cells | y+ | $CTime[s]$ $(n.cpu)$ |
|---|---|---|---|---|---|
| $L0$ | 113 | 33 | 156769 | $1-2$ | 110 (80) |
| $L1$ | 169 | 53 | 536669 | $1-2$ | 225 (128) |
| $L2$ | 209 | 73 | 1244133 | $1-2$ | 435 (192) |
| $L3$ | 249 | 93 | 2241801 | $1-2$ | 837 (224) |
| $L4$ | 305 | 113 | 4253889 | $1-2$ | 1588 (256) |

Table 2: MLMC 4-levels grid hierarchy for the ROTOR-37 problem. $CTime[s]$ is the real time in seconds required to compute one deterministic simulation on the prescribed number of cpus.

We ensure an appropriate refinement near the small tip clearance (0.356 $[mm]$) and ensure that near the boundaries the $y+$ is between 1 and 2, for all the grid levels, to accommodate the requirements of Spalart-Allmaras turbulence model employed in the CFD simulations. In Table 2 we report the number of nodes set on the blade section and spanwise on each level. The number of nodes in the perpendicular direction to the blade surface is set proportional to the number of spanwise nodes, and their distribution has a fixed grow rate. In the Fig. 2 we observe a good agreement between the computational results obtained with the finest grid level (L4) and experimental measurements of Reid and Moore [13]. The significant differences between numerical results and measurements are in the rotor stall region. For this reason we will only consider operating points before stall conditions ($\dot{m} > 20.5$ $[kg/s]$).

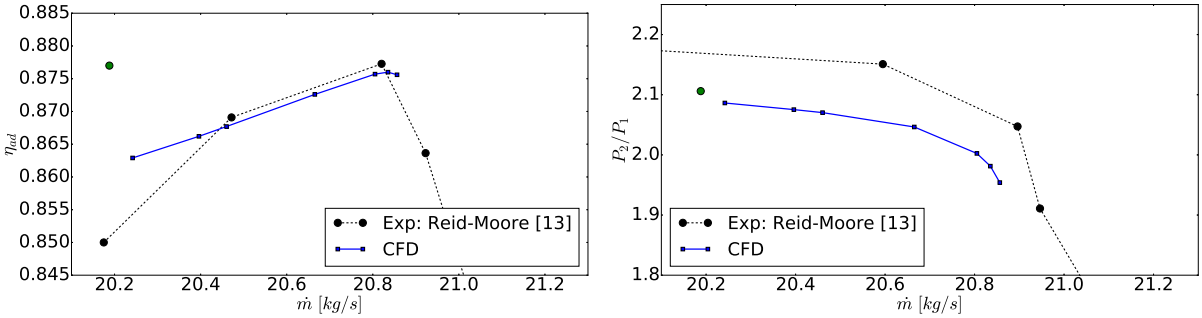


(a) Rotor adiabatic efficiency

(b) Rotor total pressure ratio

Figure 2: Experimental and computational compressor maps of the ROTOR-37. The green circles indicate the design parameters presented in the previous table.

Fig. 3 presents the flow features on the suction and pressure side of the blade and at 50% of the span for the maximum adiabatic efficiency conditions ($\eta_{ad} = 0.876$). We distinguish the bow shock at the leading edge of the blade and a classical $\lambda-$shock region (Fig. 3(g)) on the suction side where the shock impacts the boundary layer. Downstream of the shock-boundary layer interaction we identify a flow separation region. Such separation can be inferred also by looking at the skin friction (Fig. 3(c)), the boundary layer transition and at the turbulence index (Fig. 3(e)) at the wall. Additionally the boundary layer transition induces a sudden increase of eddy viscosity (Fig. 3(h)).

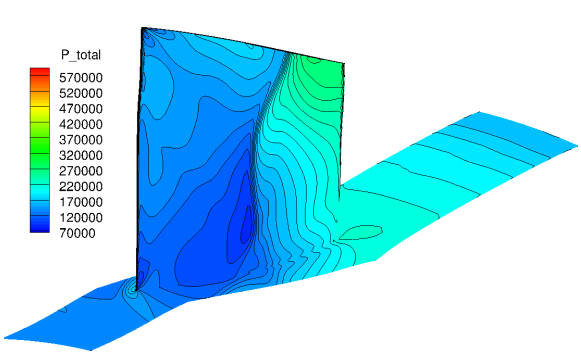


(a) Total pressure ($Pa$) - blade suction side

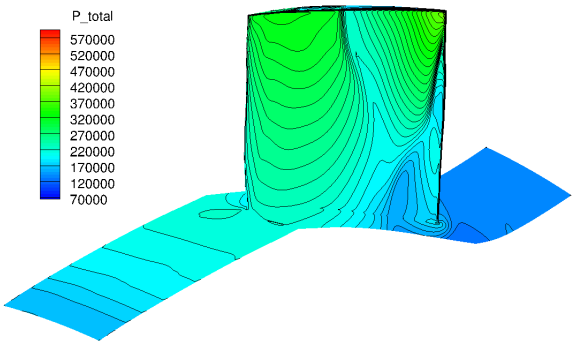


(b) Total pressure ($Pa$) - blade pressure side

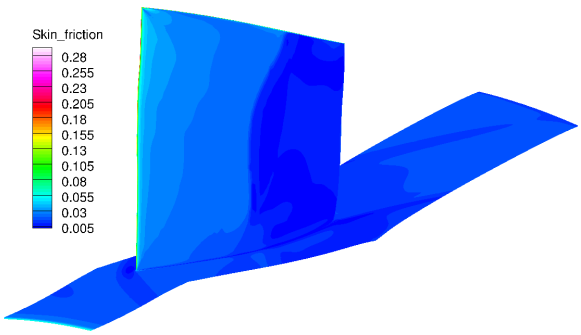


(c) Skin friction - blade suction side

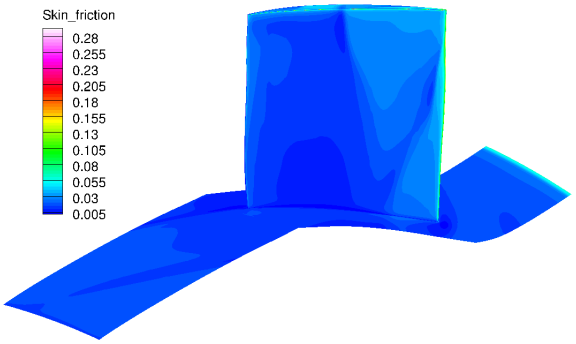


(d) Skin friction - blade pressure side

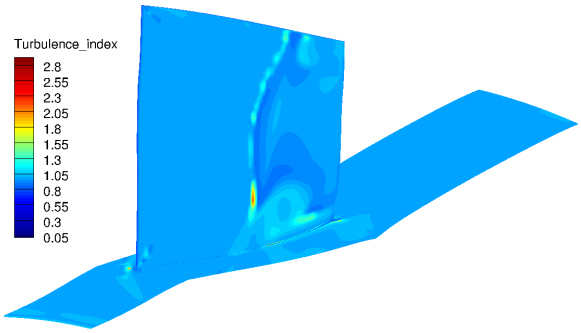


(e) Turb. index - blade suction side

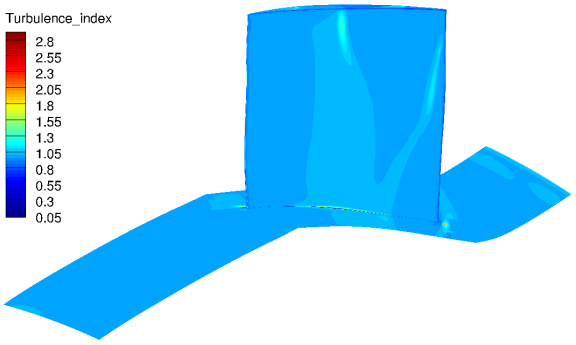


(f) Turb. index - blade pressure side

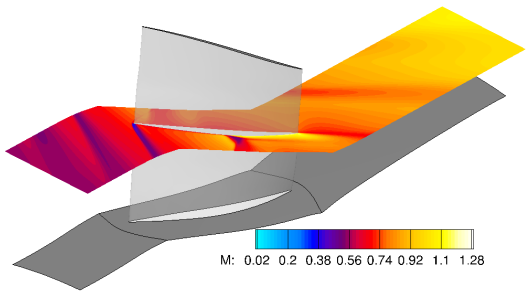


(g) Mach number - 50% span

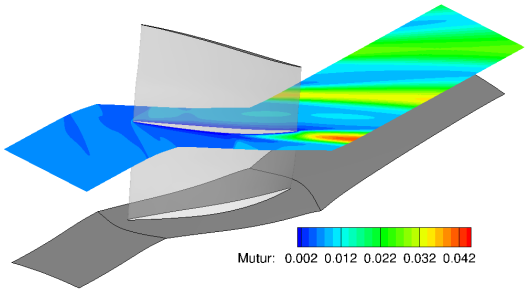


(h) Eddy viscosity - 50% span

Figure 3: Deterministic results for the ROTOR-37. Left: suction side; right: pressure side.

*4.1.2. Stochastic Results using C-MLMC*

After assessing the validity of the CFD model we now propagate uncertainties to study their effects on the performances of the rotor using the C-MLMC approach presented in section 2. We consider operating uncertainties in the inlet total pressure and total temperature profile and the outlet static pressure. The uncertainties on the parameters are modeled as truncated Gaussian random variables where we use the notation $y \sim \mathcal{TN}(\mu, \sigma^2, a, b)$ to denote a r.v. with density function

$$p(y) = \begin{cases} 0 & y < a \\ \frac{1}{z}\frac{1}{\sqrt{2\pi}\sigma} e^{-\frac{(y-\mu)^2}{2\sigma^2}} & a \leq y \leq b \\ 0 & y > b. \end{cases} \qquad \text{and} \qquad z = \int_a^b \frac{1}{\sqrt{2\pi}\sigma} e^{-\frac{(y-\mu)^2}{2\sigma^2}} dy \tag{20}$$

The following Table 3 summarizes the reference operating parameters and the uncertainties considered for the following simulations.

| | **Quantity** | **Reference** $(r)$ | **Uncertainty** $\mathcal{TN}(\mu, \sigma, X_{LO}, X_{UP})$ |
|---|---|---|---|
| INLET | $P_{tot}$ | 18 pt. profile (see Fig. 4) | $\mathcal{TN}(r, 1\%, -2\%, +2\%)$ |
| | $T_{tot}$ | 18 pt. profile (see Fig. 4) | $\mathcal{TN}(r, 1\%, -2\%, +2\%)$ |
| OUTLET | $p_o$ | $C1 = 92500.0\ [Pa]$ | $\mathcal{TN}(r, 1\%, -2\%, +2\%)$ |
| | | $C2 = 99215.0\ [Pa]$ | $\mathcal{TN}(r, 1\%, -2\%, +2\%)$ |
| | | $C3 = 110000.0\ [Pa]$ | $\mathcal{TN}(r, 1\%, -2\%, +2\%)$ |

Table 3: Operating uncertainties for the ROTOR-37 stochastic analysis.

Fig. 4 depicts the inlet uncertain total pressure and total temperature profiles. The same random perturbation from the reference profile of the total pressure and temperature is applied to every point on the inlet (fully correlated perturbation).

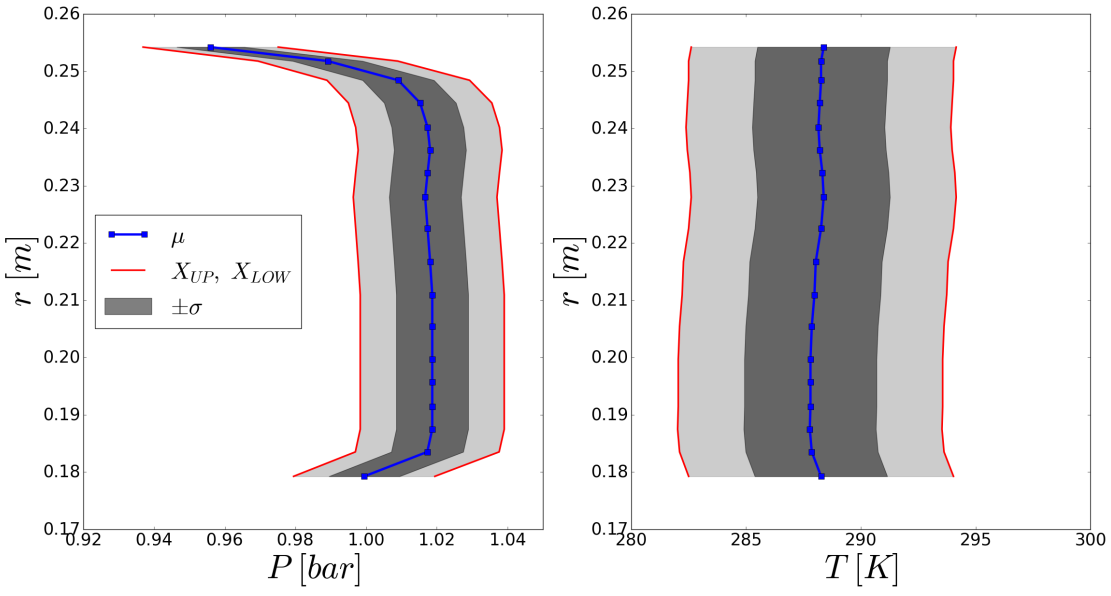


Figure 4: Uncertain total pressure and total temperature inlet profiles. The blue line represents the mean profile ($\mu$), the shaded gray area is one standard deviation ($\pm\sigma$) and the red lines are the upper and lower boundaries of the uncertain range ($X_{LOW}$, $X_{UP}$).

In Fig. 5 we present the stochastic results for the adiabatic efficiency, rotor total pressure ratio, stage total pressure ratio and mass flow for the ROTOR-37 affected by operating uncertainties (3 uncertain parameters).

For the three analyzed cases ($C1,\ C2,\ C3$ in the mean outlet pressure $p_0$) we plot the compressor map with mean $\pm$ standard deviation for the four quantities of interest. We notice that the mean values of $\dot{m}$, $\eta_{ad}$, $P_2/P_1$ and $P_3/P_1$ in the stochastic case are comparable with the deterministic ones, as observed by [14, 15]. Additionally we also observe that the mass flow $\dot{m}$ is the most sensitive quantity to variations in the operating parameters as quantified in Table 4. The variability of $\dot{m}$, $\eta_{ad}$, $P_2/P_1$ and $P_3/P_1$ seems to increase as we approach the stall conditions.

| **CASE -** $p_o$ | **Deterministic** | **Stochastic (%** $\sigma$**)** | **C-MLMC rates** |
|---|---|---|---|
| $C1 = 92500.0\ [Pa]$ | $\dot{m} = 20.8564\ [kg/s]$<br>$\eta_{ad} = 0.8756$<br>$P_2/P_1 = 1.9540$<br>$P_3/P_1 = 1.9255$ | $\dot{m} = 20.8621 \pm 0.2371\ [kg/s]\ (1.13\%)$<br>$\eta_{ad} = 0.8755 \pm 0.0009\ (0.10\%)$<br>$P_2/P_1 = 1.9534 \pm 0.0093\ (0.47\%)$<br>$P_3/P_1 = 1.9252 \pm 0.0105\ (0.54\%)$ | $\alpha = 1.7$<br>$\beta = 2.6$ |
| $C2 = 99215.0\ [Pa]$ | $\dot{m} = 20.8564\ [kg/s]$<br>$\eta_{ad} = 0.8760$<br>$P_2/P_1 = 1.9813$<br>$P_3/P_1 = 1.9559$ | $\dot{m} = 20.8440 \pm 0.2424\ [kg/s]\ (1.16\%)$<br>$\eta_{ad} = 0.8758 \pm 0.0008\ (0.09\%)$<br>$P_2/P_1 = 1.9812 \pm 0.0113\ (0.57\%)$<br>$P_3/P_1 = 1.9558 \pm 0.0106\ (0.54\%)$ | $\alpha = 1.6$<br>$\beta = 2.2$ |
| $C3 = 110000.0\ [Pa]$ | $\dot{m} = 20.6653\ [kg/s]$<br>$\eta_{ad} = 0.8726$<br>$P_2/P_1 = 2.0464$<br>$P_3/P_1 = 2.0204$ | $\dot{m} = 20.6706 \pm 0.2777\ [kg/s]\ (1.34\%)$<br>$\eta_{ad} = 0.8724 \pm 0.0010\ (0.11\%)$<br>$P_2/P_1 = 2.0451 \pm 0.0137\ (0.67\%)$<br>$P_3/P_1 = 2.0190 \pm 0.0135\ (0.67\%)$ | $\alpha = 1.8$<br>$\beta = 2.1$ |

Table 4: Deterministic and stochastic results for the ROTOR-37.

In all simulation we have imposed a relative tolerance of 0.5% on the mean value of the mass flow rate (and terminate the simulations when we achieve at least an error or the variance of the mass flow rate lower than 3%). In Table 4 we report in the last column also the estimated rates computed during the C-MLMC simulation. As it is possible to observe the statistical error decay ($\beta$) degrades as we move closer to the stall region while the lowest deterministic error decay ($\alpha$) is measured for the simulation with highest adiabatic efficiency ($C2$).

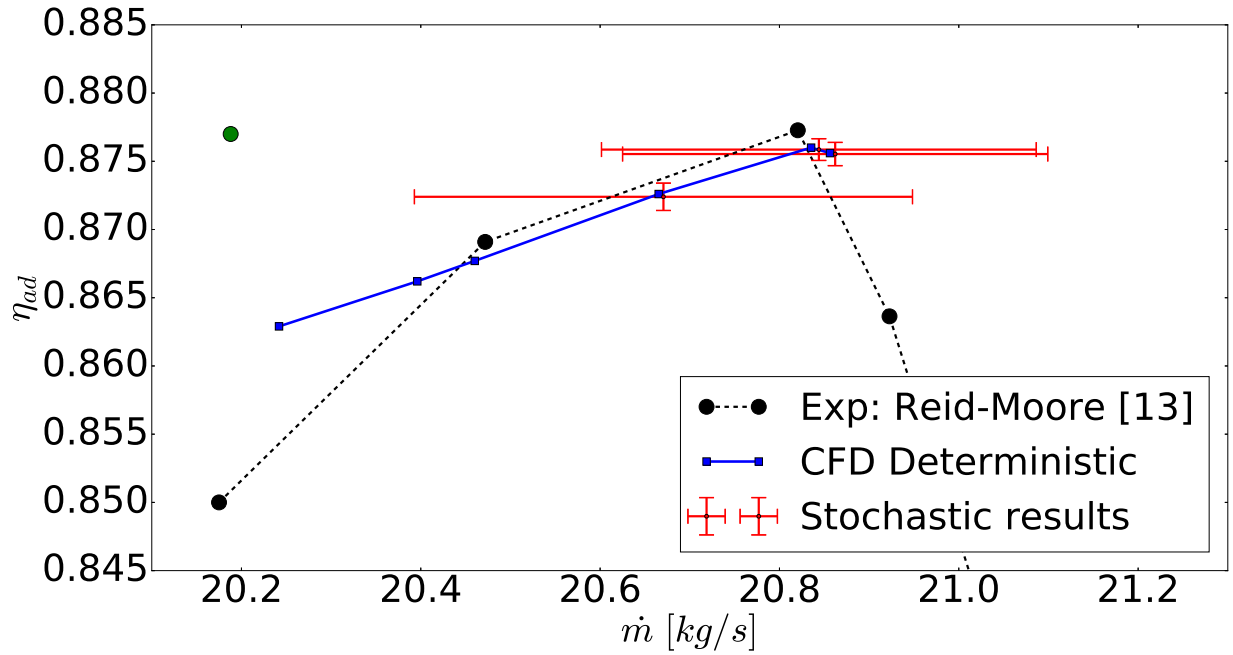


(a) Rotor adiabatic efficiency

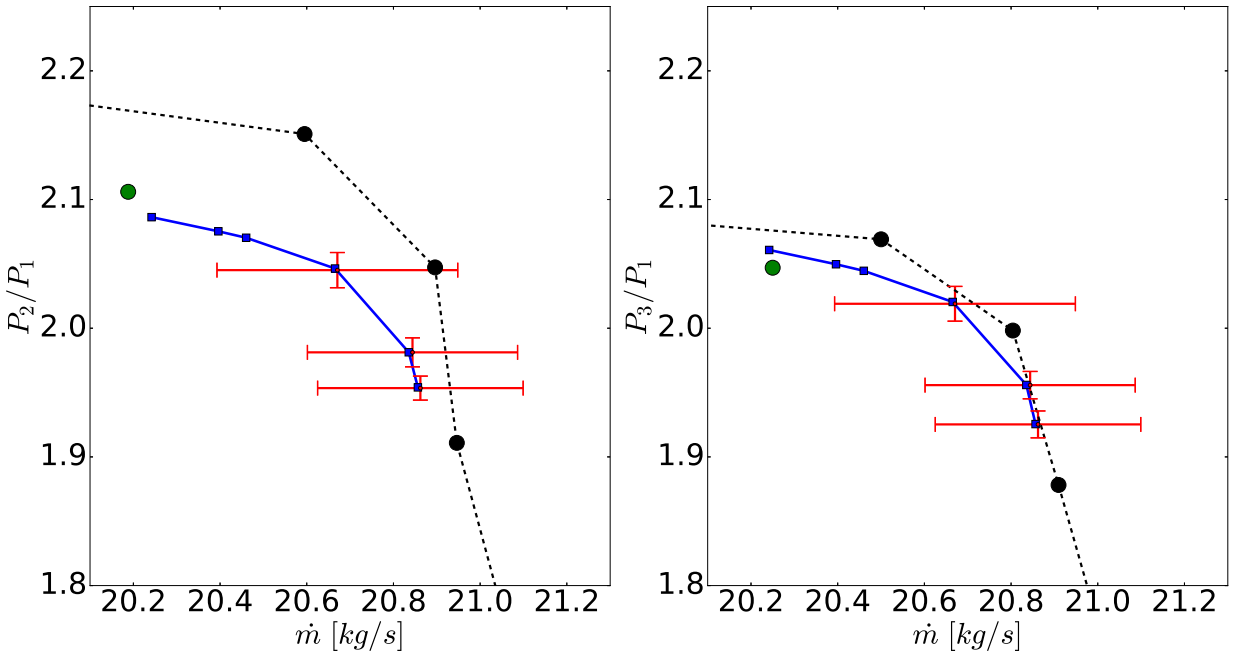


(b) Rotor total pressure ratio ($P_2/P_1$) and Stage total pressure ratio ($P_3/P_1$)

Figure 5: Experimental, deterministic and stochastic results for the compressor map of the ROTOR-37. Each red interval correspond to mean ± standard deviation.

*4.2. Model Problem: RAE2822*

The second problem we consider is the 2D RAE2822 (UMRIDA BC-02) a supercritical airfoil which has become a standard test-case for transonic flows. A detailed description of the airfoil geometry, the original experimental set-up and a series of simulations can be found in [16, 17]. For this specific problem we consider as scalar field QoI the pressure coefficient $C_p$ of the RAE 2822 affected by operating and geometric uncertainties due to fluctuations in the surrounding flow and manufacturing tolerances. The nominal geometry of the RAE2822 airfoil is defined with a set of PARSEC parameters [18]. The following table summarizes these parameters and the operating conditions considered hereafter (corrected flow conditions for case 6 in [17]).

| | **Symbol** | **Reference Value** |
|---|---|---|
| Operating | $\alpha_\infty$ | 2.31 |
| | $M_\infty$ | 0.729 |
| | $Re_c$ | $6.5 \cdot 10^6$ |
| | $p_\infty\ [Pa]$ | 101325 |
| | $T_\infty\ [K]$ | 288.5 |
| | **Symbol** | **Design Value** |
| Geometric | $R_s$ | 0.00839 |
| | $R_p$ | 0.00853 |
| | $x_s$ | 0.431 |
| | $x_p$ | 0.346 |
| | $y_s$ | 0.063 |
| | $y_p$ | $-0.058$ |
| | $C_s$ | $-0.432$ |
| | $C_p$ | 0.699 |
| | $\theta_s$ | $-11.607$ |
| | $\theta_p$ | $-2.227$ |

Table 5: Geometric and Operating reference parameters for the RAE2822 problem.

Fig. 6 illustrates the nominal geometry of the RAE 2822 and the meaning of the parameters in Table 5.

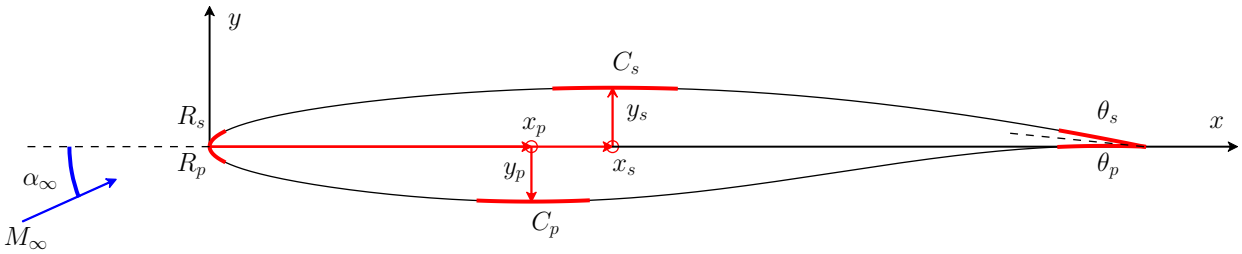


Figure 6: Geometry of the RAE 2822 transonic airfoil and PARSEC parameters that define the geometry of the airfoil.

*4.2.1. Determinsitic results*

The proprieties of the 4-levels structured C-grid hierarchy used in the C-MLMC simulations are presented in the following Table 6 and Figure 7 along with the average computational time required to compute one deterministic simulation using CFD++ software environment. A closeup view of the structured grid in the proximity of the leading edge for level 0 and level 1 is presented in Fig. 8.

As for the ROTOR-37 previous problem, we ensure that near the boundaries the $y+$ is between 1 and 2 for all the grid levels to fulfill the requirements of the Spalart-Allmaras turbulence model. In particular, we increase the number of nodes in vertical direction with respect to the airfoil (V nodes) but we require the first grid node to be always placed at the same distance ($y+$) and distribute the remaining points following a geometric grow rate. We keep the same resolution in the boundary layer but increase the density of the grid points just outside of it (Figure 8).

In Fig. 9 we compare the computational results obtained with the finest grid level (L4) and experimental measurements [17] and we observe a good agreement.

| **LEVEL** | **Airfoil nodes** | **V nodes** | **H nodes** | **Cells** | **y+** | $CTime[s]$ $(n.cpu)$ |
|---|---|---|---|---|---|---|
| $L0$ | 160 | 40 | 20 | 7722 | $1-2$ | 13.9 (16) |
| $L1$ | 320 | 80 | 40 | 31442 | $1-2$ | 49.7 (24) |
| $L2$ | 640 | 160 | 80 | 126882 | $1-2$ | 336.9 (32) |
| $L3$ | 1280 | 320 | 160 | 509762 | $1-2$ | 2145.5 (40) |
| $L4$ | 2560 | 640 | 320 | 2043522 | $1-2$ | 6854.3 (48) |

Table 6: MLMC 4-levels grid hierarchy for the RAE2822 problem. $CTime[s]$ is the real time in seconds required to compute one deterministic simulation on the prescribed number of cpus.

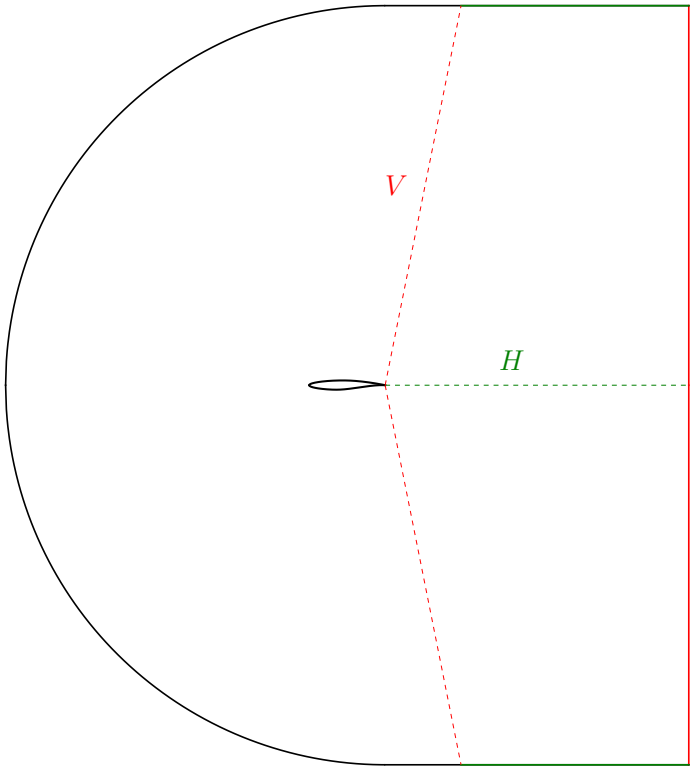


Figure 7: Details for the structured RAE-2822 grid setting.

*4.2.2. Stochastic Results using C-MLMC*

We now propagate geometric and operating uncertainties in the model to study their effects on the $C_p$ profile of the airfoil using the C-MLMC approach. We consider operating uncertainties in the far-field Mach

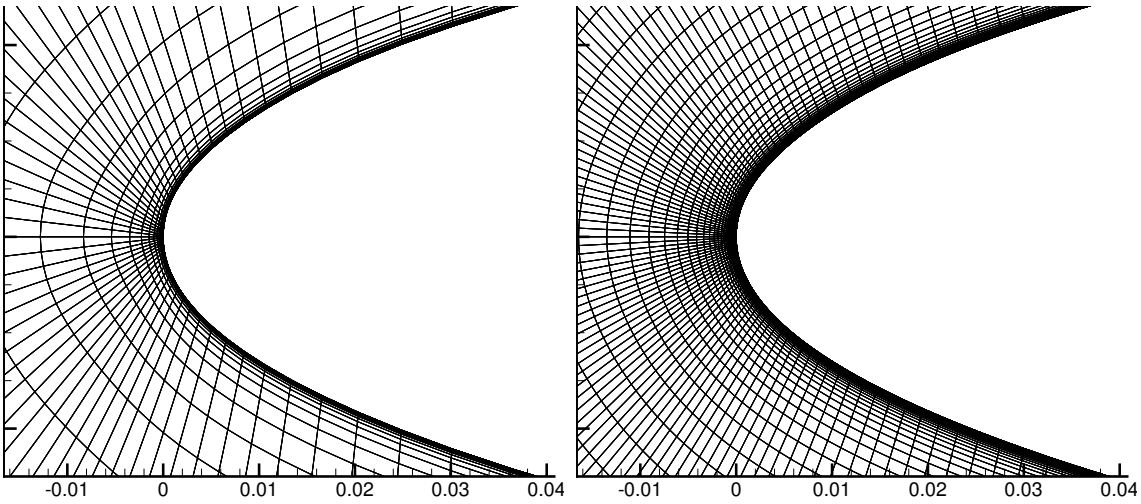


(a) $L0$ (b) $L1$

Figure 8: Leading edge closeup view of level 0 and 1 grids for the RAE2822 problem.

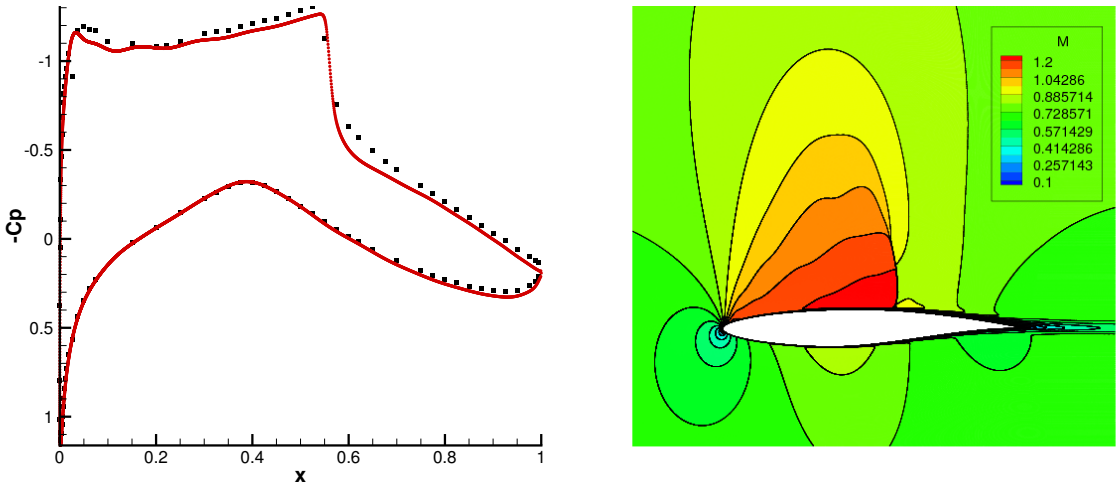


(a) Experimental (black squares) and computational (red line) $C_p$ coefficient around the airfoil

(b) Mach number

Figure 9: Deterministic results for the RAE2822 airfoil.

number and angle of attach and geometric uncertainties in the PARSEC coefficients that define the shapes of the airfoil. In case of geometric uncertainties that affect the shape of the airfoil, for each random geometry (set of PARSEC coefficients) we deform the existing grid levels by solving a linear elasticity problem on the volume grid to accommodate the new boundary definition (Fig. 10).

The following Table 7 and Fig. 11 summarize the operating and geometric parameters and their uncertainties modeled as truncated Gaussian random variables (see (20)).

In Fig. 12 we present the stochastic results for the pressure coefficient profile $C_p$ around the airfoil under operating uncertainties (2 uncertain parameters hereafter denoted as **OPER(2)**), geometric uncertainties (8 uncertainties denoted as **GEOM(8)**) and operating and geometric uncertainties at the same time (10 uncertainties denoted as **OPER(2)+GEOM(8)**) presented in Table 7.

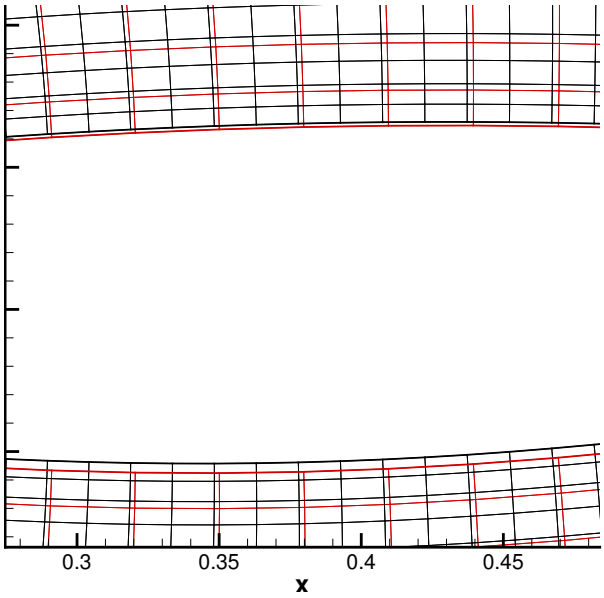


Figure 10: Grid deformation to accommodate the geometric uncertainty.

| | **Quantity** | **Reference** $(r)$ | **Uncertainty** $\mathcal{TN}(\mu, \sigma, X_{LO}, X_{UP})$ |
|---|---|---|---|
| Operating | $\alpha_\infty$ | 2.31 | $\mathcal{TN}(r, 2\%, -2\%, +2\%)$ |
| | $M_\infty$ | 0.729 | $\mathcal{TN}(r, 5\%, -5\%, +5\%)$ |
| | $Re_c$ | $6.5 \cdot 10^6$ | – |
| | $p_\infty$ $[Pa]$ | 101325 | – |
| | $T_\infty$ $[K]$ | 288.5 | – |
| Geometric | $R_s$ | 0.00839 | $\mathcal{TN}(r, 0.25\%, -1\%, +1\%)$ |
| | $R_p$ | 0.00853 | $\mathcal{TN}(r, 0.25\%, -1\%, +1\%)$ |
| | $x_s$ | 0.431 | $\mathcal{TN}(r, 0.5\%, -1\%, +1\%)$ |
| | $x_p$ | 0.346 | $\mathcal{TN}(r, 0.5\%, -1\%, +1\%)$ |
| | $y_s$ | 0.063 | $\mathcal{TN}(r, 0.5\%, -3\%, +3\%)$ |
| | $y_p$ | $-0.058$ | $\mathcal{TN}(r, 0.5\%, -3\%, +3\%)$ |
| | $C_s$ | $-0.432$ | $\mathcal{TN}(r, 0.5\%, -1\%, +1\%)$ |
| | $C_p$ | 0.699 | $\mathcal{TN}(r, 0.5\%, -1\%, +1\%)$ |
| | $\theta_s$ | $-11.607$ | – |
| | $\theta_p$ | $-2.227$ | – |

Table 7: Operating and geometric uncertainties for the RAE2822 stochastic analysis.

The decay rates of deterministic and statistical error computed during the C-MLMC analysis are $\alpha = 0.7,\ \beta = 1.06$ for the case with only operating uncertainties (**OPER(2)**) and $\alpha = 0.6,\ \beta = 1.05$ for that with operating and geometric uncertainties (**OPER(2)+GEOM(8)**).

Lastly we present in Fig. 13 the level sample sizes at each iteration of the C-MLMC algorithm to achieve a relative error $\varepsilon_r = 0.6\%$ on the L2 norm of the pressure coefficient for the **OPER(2)** and **OPER(2)+GEOM(8)** cases. Additionally we compare the aggregate cost (total CPU time) required by our implementation of C-MLMC with the MC method to achieve a RMSE of $\varepsilon$. Notice how the performace of the C-MLMC is only mildly affected by the number of uncertain parameters. Moreover for the target relative tolerance $\varepsilon_r = 0.6\%$ the gain in computational cost of C-MLMC over MC is about 2 orders of magnitude and is expected to increase even further if smaller tolerances are prescribed. The results match nicely the

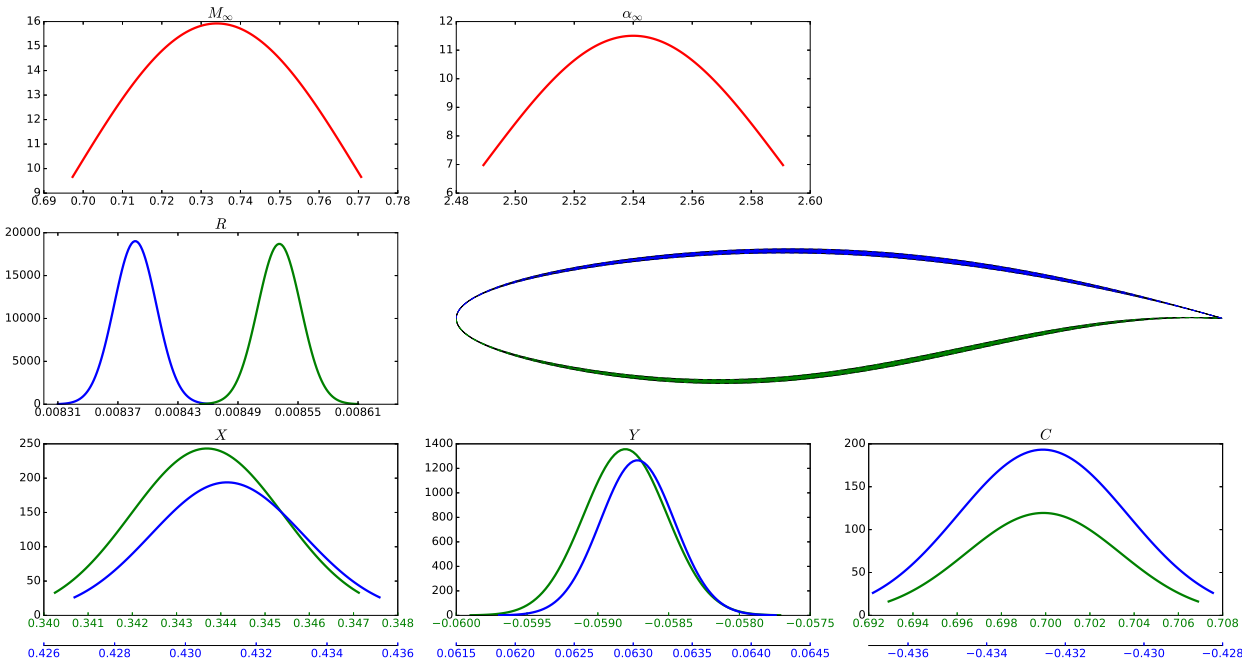


Figure 11: Probability density functions of the operating (red) and geometric (blue suction side and green pressure side) parameters for the RAE2822 stochastic analysis.

theoretical estimates.

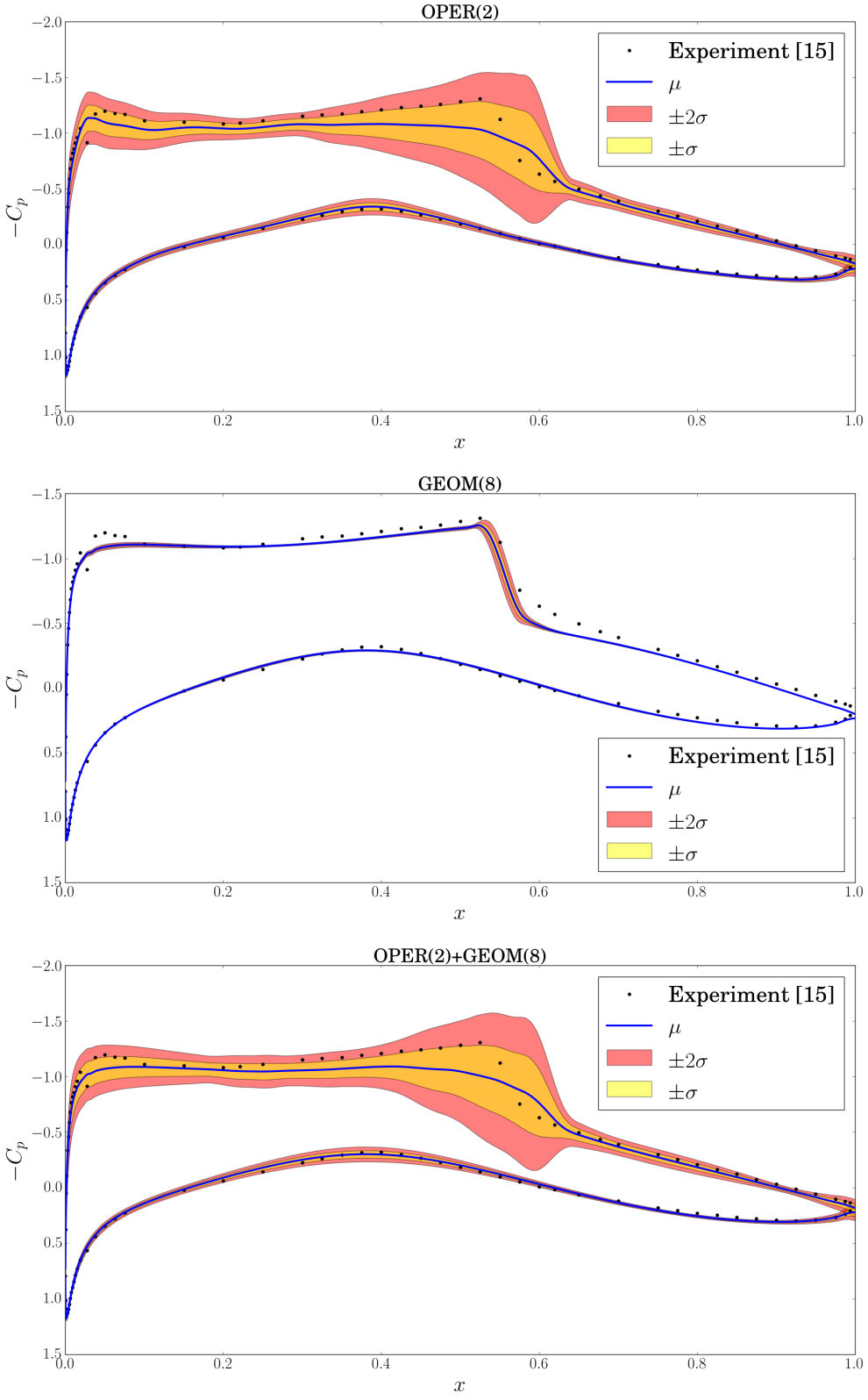


Figure 12: UQ analysis results for the RAE2822 presenting the mean pressure coefficient profile around the airfoil and its standard deviation. Experimental data from [17].

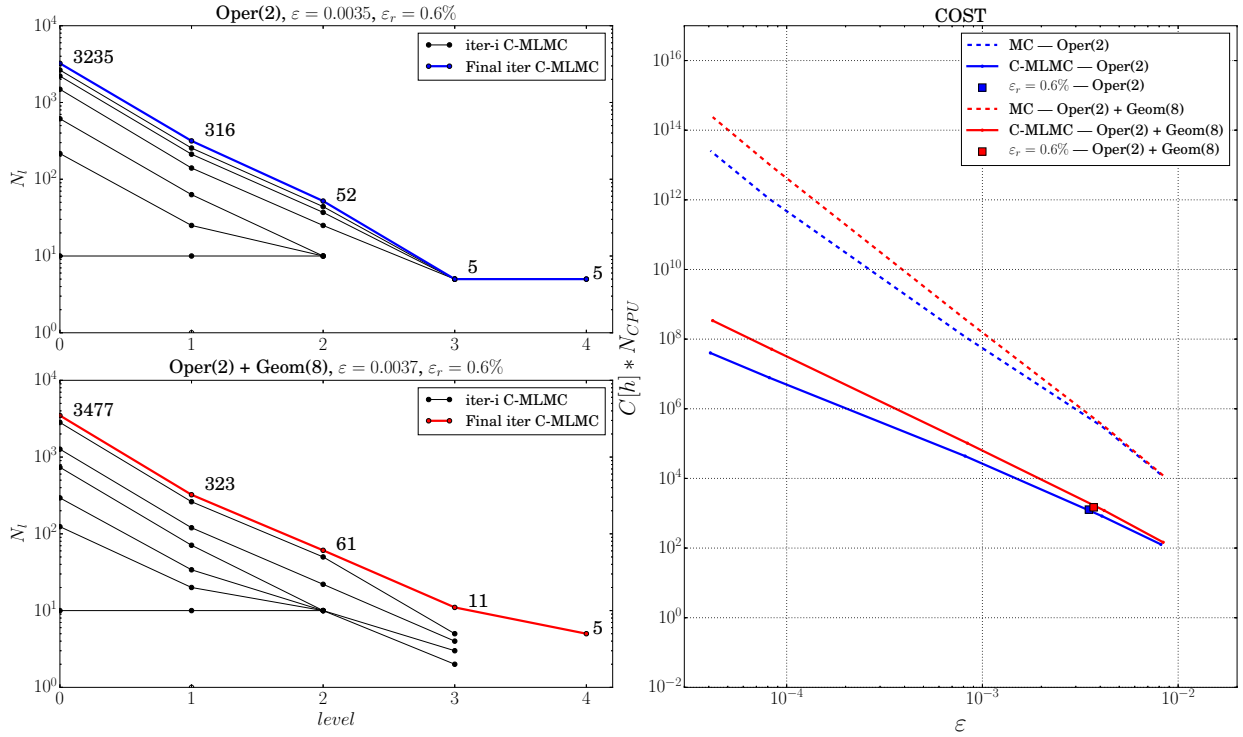


Figure 13: C-MLMC hierarchies for two different sets of uncertain parameters (left) and aggregate computational cost compared with MC (right). The solid lines in the cost plot are an extrapolated model based on the rates and constants ($\alpha$. $c_\alpha$, $\beta, c_\beta, \gamma, c_\gamma$) fitted in C-MLMC. The red and blue squares are the actual computed cost and error in the C-MLMC simulations.

## Acknowledgments

This research has received funding from the European Union's Seventh Framework Programme for research, technological development and demonstration under grant agreement no ACP3-GA-2013-605036 (Uncertainty Management for Robust Industrial Design in Aeronautics (UMRIDA) project). The first two authors acknowledge also support from the Center for ADvanced MOdeling Science (CADMOS).

## Bibliography

[1] Pisaroni, M., Nobile, F., Leyland, P.: A continuation multi level monte carlo (c-mlmc) method for uncertainty quantifcation in compressible aerodynamics. Technical report (2016)
[2] Collier, N., Haji-Ali, A.L., Nobile, F., von Schwerin, E., Tempone, R.: A continuation Multilevel Monte Carlo algorithm. BIT Numerical Mathematics (2014) 1–34
[3] Giles, M.B.: Multilevel Monte Carlo path simulation. Operations Research **56**(3) (2008) 607–617
[4] Pisaroni, M., Leyland, P., Nobile, F.: A Multi Level Monte Carlo algorithm for the treatment of geometrical and operational uncertainties in internal and external aerodynamics. In: 46th AIAA Fluid Dynamics Conference. (2016) 4398
[5] Barth, A., Schwab, C., Zollinger, N.: Multi-level Monte Carlo finite element method for elliptic PDEs with stochastic coefficients. Numerische Mathematik **119**(1) (2011) 123–161
[6] Cliffe, K., Giles, M., Scheichl, R., Teckentrup, A.L.: Multilevel Monte Carlo methods and applications to elliptic PDEs with random coefficients. Computing and Visualization in Science **14**(1) (2011) 3–15
[7] Barth, A., Lang, A., Schwab, C.: Multilevel Monte Carlo method for parabolic stochastic Partial Differential Equations. BIT Numerical Mathematics **53**(1) (2013) 3–27
[8] Charrier, J., Scheichl, R., Teckentrup, A.L.: Finite element error analysis of elliptic PDEs with random coefficients and its application to Multi level Monte Carlo methods. SIAM Journal on Numerical Analysis **51**(1) (2013) 322–352
[9] Gatski, T.B., Bonnet, J.P.: Compressibility, turbulence and high speed flow. Academic Press (2013)
[10] Hirsch, C.: Numerical computation of internal and external flows: The fundamentals of computational fluid dynamics. Butterworth-Heinemann (2007)
[11] Mani, M., Babcock, D., Winkler, C., Spalart, P.: Predictions of a supersonic turbulent flow in a square duct. AIAA Paper **860** (2013)
[12] Dunham, J.: CFD validation for propulsion system components (la validation cfd des organes des propulseurs). Technical report, DTIC Document (1998)
[13] Reid, L., Moore, R.D.: Design and overall performance of four highly loaded, high speed inlet stages for an advanced high-pressure-ratio core compressor. NASA Technical Report (1978)
[14] Loeven, G., Bijl, H.: The application of the probabilistic collocation method to a transonic axial flow compressor. American Institute of Aeronautics and Astronautics (AIAA) (2010)
[15] Gopinathrao, N.P., Bagshaw, D., Mabilat, C., Alizadeh, S.: Non-deterministic cfd simulation of a transonic compressor rotor. In: ASME Turbo Expo 2009: Power for Land, Sea, and Air, American Society of Mechanical Engineers (2009) 1125–1134
[16] Haase, W., Brandsma, F., Elsholz, E., Leschziner, M., Schwamborn, D.: EUROVAL An European Initiative on Validation of CFD Codes: Results of the EC/BRITE-EURAM Project EUROVAL, 1990–1992. Volume 42. Springer-Verlag (2013)
[17] V.A.: EXPERIMENTAL DATA BASE FOR COMPUTER PROGRAM ASSESSMENT - Report of the Fluid Dynamics Panel Working Group. AGARD-AR-138 (1979)
[18] Sobieczky, H.: Parametric Airfoils and Wings. Notes on Numerical Fluid Mechanics, edited by K. Fujii and G.S. Dulikravich **68** (1998) 71–88